Effects of Vegetation Patch Patterns on Channel Morphology

A Numerical Study

Li, Jiaze; Claude, Nicolas; Tassi, Pablo; Cordier, Florian; Vargas-Luna, Andrés; Crosato, Alessandra; Rodrigues, Stéphane

DOI
10.1029/2021JF006529

Publication date
2022

Document Version
Final published version

Published in
Journal of Geophysical Research: Earth Surface

Citation (APA)
Li, J., Claude, N., Tassi, P., Cordier, F., Vargas-Luna, A., Crosato, A., & Rodrigues, S. (2022). Effects of Vegetation Patch Patterns on Channel Morphology: A Numerical Study. *Journal of Geophysical Research: Earth Surface*, *127*(5), Article e2021JF006529. https://doi.org/10.1029/2021JF006529

JGR Earth Surface

RESEARCH ARTICLE
10.1029/2021JF006529

Effects of Vegetation Patch Patterns on Channel Morphology: A Numerical Study

Jiaze Li[1,2,3], Nicolas Claude[4], Pablo Tassi[1,2], Florian Cordier[1], Andrés Vargas-Luna[5], Alessandra Crosato[6,7], and Stéphane Rodrigues[3,8]

[1]EDF R&D – National Laboratory for Hydraulics and Environment (LNHE), Chatou, France, [2]Saint-Venant Laboratory for Hydraulics, Chatou, France, [3]UMR CNRS CITERES, University of Tours, Tours, France, [4]EDF, Centre Ingénierie Hydraulique, La Motte Servolex, France, [5]Department of Civil Engineering, Pontificia Universidad Javeriana, Bogotá, Colombia, [6]Faculty of Civil Engineering and Geosciences, Delft University of Technology, Delft, The Netherlands, [7]Department of Water Resources and Ecosystems, IHE Delft Institute for Water Education, Delft, The Netherlands, [8]Graduate School of Engineering Polytech Tours, University of Tours, Tours, France

Abstract This study investigates the effects of vegetation patch patterns on the morphological evolution of alluvial river channels at the reach-scale. For this, a new two-dimensional numerical biomorphodynamic model has been developed using the Telemac-Mascaret system. Considering the newest development in the topic, the effects of vegetation on bedload transport are included by extending Einstein's parameters for the sediment transport formula. The model was subsequently validated by published laboratory experiments reproducing alternate bar dynamics with different vegetation establishment scenarios. The validated model was then used to study the influence of vegetation patch patterns on the channel morphological evolution considering the two most observed ones: (a) the filled pattern with plants well distributed within the patch, and (b) the stripe pattern with plants established only along the patch edges. 14 scenarios were simulated in total, including sensitivity analyses on the coefficients of vegetation characteristics. The results indicate that the morphological responses of an alternate bar system to the stripe pattern consist of channel widening, steeper slope and reduced water depth, with increased sediment transport rates. The effects of the filled pattern are similar but weaker. The results also show that with the stripe pattern, the alternate bars tend to migrate toward the centerline forming center bars. Besides, the scroll bars forming downstream are shorter, corresponding to less visible chute channels, compared to the filled pattern. Despite much less vegetation coverage, the stripe pattern decreases the bar elongation rates in a way similar to the filled pattern.

Plain Language Summary Vegetation influences river morphological evolution by reducing the flow velocity thus the sediment transport capacity of flowing water. Many studies have been carried out to investigate the influence of physical characteristics of uniformly distributed vegetation such as plant height, diameter, density, etc. However, the spatial distribution of vegetation in nature is generally presented as patches (an area of vegetation surrounded by bare soil) due to environmental factors. In this study, we developed a numerical model to investigate the effects of vegetation patch patterns on the channel morphological evolution considering the two most observed ones: (a) the filled pattern with plants well distributed within the patch, and (b) the stripe pattern with plants only aligned on the patch contour. The numerical results show that the channel morphological responses of two patch patterns present the same evolution tendency but with different rates. Besides, the stripe patch controls bar (an elevated region of sediment in the river) elongation rates, similar to the densely vegetated filled patch with the same contour line. This study provides new insights into the importance of the spatial distribution of vegetation for fluvial morphology evolution and helps to conceive river restoration management such as vegetation removal scenarios to remobilize vegetated river bars.

Key Points:

- A numerical model considering the effects of vegetation on bedload sediment transport by extending Einstein's parameters is validated against laboratory experiments
- Morphological responses to filled and stripe patterns show similarities in chute channel formation and differences in reach-scale channel characteristics
- Patches with plants located only along the patch edge control bar elongation similarly to densely vegetated patches at the same elevation

Supporting Information:

Supporting Information may be found in the online version of this article.

Correspondence to:

J. Li,
jiaze.li@edf.fr

Citation:

Li, J., Claude, N., Tassi, P., Cordier, F., Vargas-Luna, A., Crosato, A., & Rodrigues, S. (2022). Effects of vegetation patch patterns on channel morphology: A numerical study. *Journal of Geophysical Research: Earth Surface*, *127*, e2021JF006529. https://doi.org/10.1029/2021JF006529

Received 20 NOV 2021
Accepted 26 APR 2022

Author Contributions:

Conceptualization: Jiaze Li, Nicolas Claude, Pablo Tassi, Florian Cordier, Alessandra Crosato, Stéphane Rodrigues
Data curation: Andrés Vargas-Luna
Methodology: Jiaze Li, Nicolas Claude, Pablo Tassi, Florian Cordier, Stéphane Rodrigues
Resources: Nicolas Claude, Andrés Vargas-Luna
Software: Jiaze Li, Florian Cordier
Supervision: Nicolas Claude, Pablo Tassi, Florian Cordier, Alessandra Crosato, Stéphane Rodrigues
Validation: Jiaze Li, Pablo Tassi, Florian Cordier, Andrés Vargas-Luna, Alessandra Crosato

1. Introduction

By acting as a passive role (Camporeale et al., 2013), aquatic vegetation increases the local hydraulic roughness (Baptist, 2005; Tsujimoto, 1999), reduces the flow velocity, the bed shear stress and the sediment transport capacity of flowing water (Bennett et al., 2002; Le Bouteiller & Venditti, 2014). In river systems, riparian and floodplain vegetation acts as an ecosystem engineer (Gurnell, 2014; Jones et al., 1997), influencing channel patterns and river morphodynamic processes in a way that favors the colonization of new plants (Bertoldi et al., 2015; Hickin, 1984; Tal & Paola, 2010; Vargas-Luna, Duró, et al., 2019). For instance, the pioneer plants that colonize

Visualization: Jiaze Li, Andrés Vargas-Luna
Writing – original draft: Jiaze Li
Writing – review & editing: Jiaze Li, Nicolas Claude, Pablo Tassi, Florian Cordier, Andrés Vargas-Luna, Alessandra Crosato, Stéphane Rodrigues

the emerging parts of river channels (banks and bar tops) trap fine sediment, rich in nutrients, and decrease the flow velocity during high-flow stages, reducing local bed erosion and plant removal, promoting thus the establishment of new plants (Corenblit et al., 2016, 2020). On the other hand, the river dynamics strongly influence seedling establishment (Caponi et al., 2019; Mahoney & Rood, 1998) and thus the spatial distribution of vegetation (Zhou et al., 2018), with plant mortality dominated by inundation, desiccation (Johnson, 2000), burial (Kui & Stella, 2016) and uprooting (Bywater-Reyes et al., 2015; Edmaier et al., 2011; Wintenberger et al., 2019).

Laboratory experiments of vegetated channels have allowed describing the interactions between flow and sediment transport for various plant characteristics, under emergent or submerged conditions. Based on laboratory data, algorithms have been formulated to derive, for instance, the local flow resistance and the bed-load rate as a function of vegetation characteristics (e.g., Armanini & Cavedon, 2019; Bonilla-Porras et al., 2021; Murphy et al., 2007; Nepf, 1999; Nepf & Vivoni, 2000). However, vegetation distribution in nature is not uniform and plants are grouped to form patches, that is, high plant density regions surrounded by bare ground. Several studies (e.g., Kondziolka & Nepf, 2014; Schwarz et al., 2018; Van Dijk et al., 2013) suggest that the spatial distribution of vegetation strongly affects the morphological evolution and further the landscape patterns of aquatic systems.

Several attempts have been made in the laboratory and in the field to study the flow characteristics (Li et al., 2019; Zong & Nepf, 2012) and the spatial sedimentation and erosion patterns (Bouma et al., 2007; Euler et al., 2014; Follett & Nepf, 2012; Zong & Nepf, 2011) within and around vegetation patches. The laboratory experiments of Bennett et al. (2002) showed that near-bank vegetation patches can deflect the flow toward the opposite bank, reducing flow velocity near and within the patches. Later, Bennett et al. (2008) studied the morphological responses to three different forms of near-bank vegetation patches (rectangular, square, and semicircular) placed in a straight channel with erodible banks for restoration of river meanders. Similarly, Kim et al. (2015, 2019) investigated the flow pattern and the morphological changes around a rectangular patch along the sidewall of a flume and in a channel with erodible banks. They found that the spatial erosion and deposition around and within the vegetation patch can be closely related to the hydraulic conditions and the obstruction ratio, length, density, and submergence ratio of the patch.

Several three dimensional (3D) numerical studies have been carried out to analyze the flow structure and the sediment dynamics at stem scale around obstacles, such as bridge piers (Khosronejad et al., 2012; Nagata et al., 2005), or near vegetation patches (Bouma et al., 2007). The results of these studies show that a strong vortex structure develops near the bed forming a scour hole around the obstacle. Furthermore, investigations dealing with vegetation patches demonstrated the influence of vegetation on wave attenuation and flow velocity reduction within the patch (Marsooli & Wu, 2014). However, a 3D numerical model requires tremendous computation time for a larger domain such as at reach-scale. Focusing on larger spatial scales, the two-dimensional hydrodynamic model of Leu et al. (2008) used five vegetation patch configurations to investigate the effects of vegetation cutting on water flow. Their results suggest that cutting vegetation along the main channel side is the most effective measure to reduce water depths and flow velocities. Guan and Liang (2017) developed a 2D hydro-morphological model including a parameterization of vegetation shear stress to simulate the channel pattern adjustment to vegetation patches. In their model, the effects of flexible plants (e.g., grass) are represented by increasing hydraulic roughness and the ones of rigid plants (e.g., trees) are represented by adding a drag force. To examine the influence of geometry and plant density of near-bank vegetation patches on morphological adjustment, Xu et al. (2019) built and validated a hydro-morphological model based on flume experiments. They found that the increase in vegetation density, patch length and width leads to stronger flow blockage effects encouraging the growth of the pool region adjacent to the patch. Bywater-Reyes et al. (2018) built a two-dimensional hydraulic model on a point bar with a vegetation patch forming in nature, using FaSTMECH, a model contained within the iRIC platform, downloadable from https://i-ric.org/en/ (Shimizu et al., 2020). Bywater-Reyes et al. (2018) analyzed the impact of vegetation over a point bar on channel-bend flow dynamics under different discharges, vegetation densities, and plant morphologies.

In an attempt to better understand naturally occurring vegetation patches, Meron (2019) analyzed the mechanisms of vegetation patch pattern formation and distinguished five basic patterns: uniform vegetation, gap pattern, stripe pattern, spot pattern, and bare soil. Many studies (e.g., Caponi et al., 2019; Džubáková et al., 2015; Wintenberger et al., 2019) have observed that vegetation distribution is uniformly located on bar tops forming a filled patch pattern. Besides, *In-situ* observations of Corenblit et al. (2016) on *Populus nigra L.* on alluvial bars of the Garonne River in France demonstrated that young cohorts often grow in stripes next to the water. The field surveys of Zhou

et al. (2018) on the Suzuka River in Japan showed as well that the initial vegetation establishment locations over bars are along the wet/dry area near the border, forming a stripe pattern. Gurnell and Bertoldi (2020) investigated the effects of *Alnus incana* and *Populus nigra* on islands and floodplain development of the Tagliamento River in Italy, and they found that *A. incana* is mainly distributed in lines along the border of channels and bars.

However, there has been no specific, controlled study to investigate the effects of vegetation patch patterns on fluvial processes. As a result, the role of different vegetation patch patterns on the morphodynamics of alluvial channels is not yet well understood. Besides, previous studies on near-bank vegetation patches use static, uniform cylinders as vegetation, where ecological processes and biomorphodynamics interactions are poorly represented. Vegetation patch patterns are schematized through simple un-realistic shapes, such as circular, semi-circular, and rectangular configurations, with plants only uniformly distributed within the patches.

The objective of the present study is to provide a general understanding of the role of two common vegetation patch patterns on fluvial processes (filled and stripe) at the reach-scale. For this purpose, a 2D numerical biomorphodynamic model is developed, coupling a hydrodynamics module based on the solution of the shallow water equations, a sediment mass balance equation for the bed evolution and a vegetation dynamics model (Jourdain et al., 2020). To include the effects of vegetation on sediment transport, assumed as bedload, extended Einstein's parameters are applied to the formula of Van Rijn (1984), as recently suggested by Armanini and Cavedon (2019) and Bonilla-Porras et al. (2020), revised by Bonilla-Porras et al. (2021). The numerical model is calibrated and validated against the laboratory experiments of Vargas-Luna, Duró, et al. (2019), which were carried out in a mobile-bed flume with erodible banks, floodplains and high terraces. Using grassy-type plastic plants, Vargas-Luna, Duró, et al. (2019) considered three scenarios: without vegetation, with vegetation on floodplains, and with vegetation on both floodplains and areas emerging at low flows, namely alternate bar tops, to analyze the effects of vegetation on the morphological evolution of the system. To examine and compare the effects of vegetation patch patterns, the two most observed patch patterns: filled pattern (with uniformly distributed vegetation within the patch), and stripe pattern (with vegetation only aligned along the patch contour) are investigated in this study. The numerical results show that channel morphological responses to those two different vegetation patches present similarities in chute channel formation and differences in channel characteristics at the reach-scale. Besides, this work demonstrates the importance of the spatial distribution of vegetation patches on bar elongation rates.

2. Materials and Methods

2.1. Study Case

The numerical model implemented in this work is based on the large-scale laboratory experiment conducted by Vargas-Luna, Duró, et al. (2019) at the Environmental Fluid Mechanics Laboratory of the Delft University of Technology, investigating the effects of vegetation on riverbed evolution and channel planform. The experimental flume was 45 m long and 5 m wide (Figure 1a). The initial configuration (Figure 1b) corresponded to a channel (0.80 m wide and 0.15 m deep) excavated through a thick sand layer, with floodplains (1 m wide) and high terraces (1.1 m wide) on both sides. A reservoir at the end of the flume regulated the downstream water level and allowed recirculation of the water-sediment mix during the experiments. The upstream inlet structure contained a 0.4 m long transverse plate (half initial channel width) to generate a sequence of alternate bars. Discounting the upstream and downstream structures, the effective flume length was 36 m long (see Figure 1b). The sand composition (Figure 1c) was selected based on the results of previous experiments by Vargas-Luna, Crosato, et al. (2019), in which the median sediment size $D_{50} = 0.001$ m and the sorting index I was equal to 2.26, given as:

$$I = 0.5\left(\frac{D_{84}}{D_{50}} + \frac{D_{50}}{D_{16}}\right) \tag{1}$$

where D_x is the diameter of the sediment exceeding x percentage of the material (m).

The artificial plants (Figure 1d) used in the experiment were composed of 0.03 m high plastic tussocks (tufts of grass) with wooden sticks root of 0.07 m long. The diameters of the tussocks and the roots were 0.022 and 0.002 m, respectively. Plants were planted manually on the floodplains and over the emerging bar tops, with a density of 112 plants per square meter in a staggered pattern. The plants used in the experiments behaved as rigid under the experimental flow conditions.

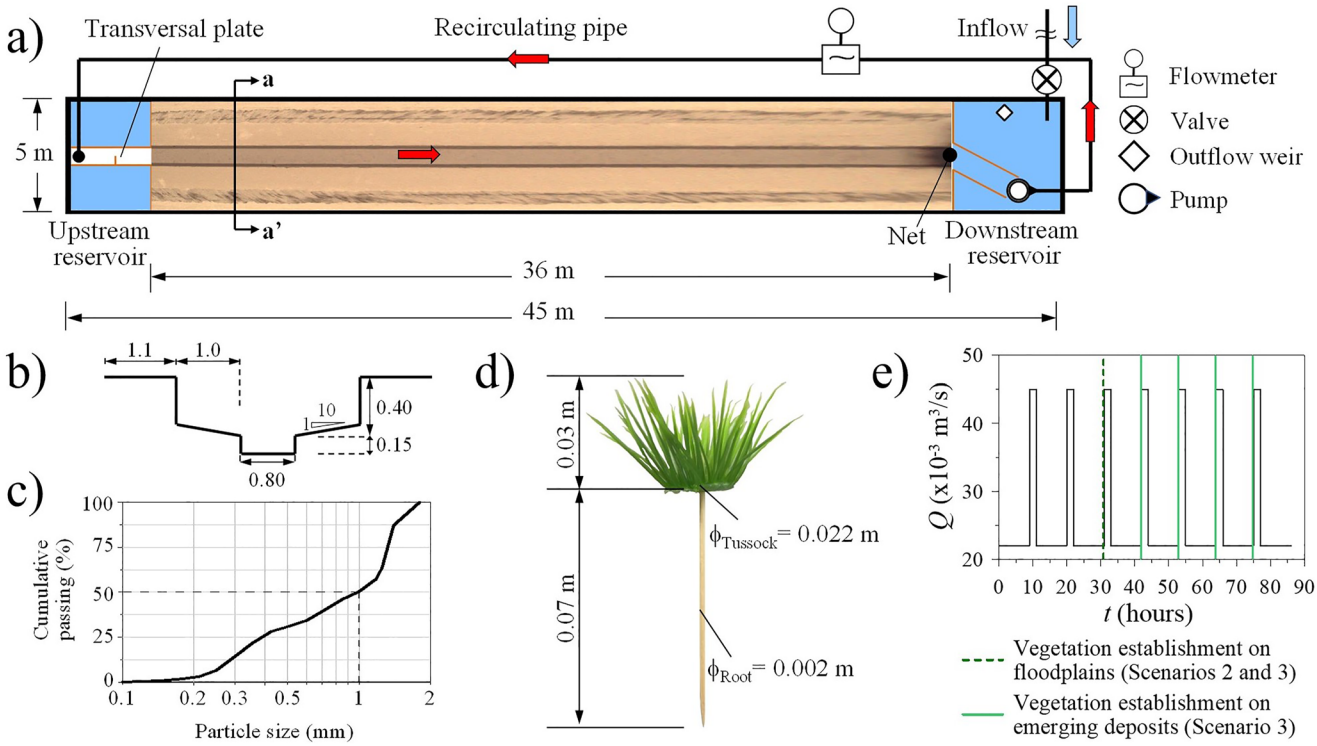

Figure 1. Experimental setup of Vargas-Luna, Duró, et al. (2019): (a) planview of the flume, (b) initial cross-section a-a' identified in the planview, with main channel, floodplains and high terraces, (c) grain size distribution of the non-uniform sediment, (d) artificial tussocks, and (e) discharge hydrograph indicating the vegetation colonization moments. All measures are shown in meters.

The flow regime (Figure 1e) consisted of a series of low and high discharges of 22 and 45 l/s for 9 and 2 hr, respectively. The experiments had a total duration of 86 hr, with the first stage for alternate bar formation without vegetation of 31 hr, and a second stage with or without vegetation of 55 hr. Three scenarios were studied (Figure 1e): (a) without vegetation for 86 hr; (b) vegetation placed on the floodplains after 31 hr (at the end of the first stage); (c) vegetation placed on the floodplains after 31 hr and subsequently on emerging bar tops at the end of each low flow stage.

2.2. Mathematical Model and Numerical Solution

The hydrodynamic module is based on the solution of the horizontal, depth-averaged shallow-water equations (de Saint-Venant, 1871; Hervouet, 2007), expressed in a Cartesian reference system (*x, y, z*). The governing equations for hydrodynamics are completed with closure relationships for the bed resistance and turbulence. For the former, a squared function dependency on the depth-averaged component of velocity is used, where the friction coefficient is specified with the Nikuradse formula (1950). For the latter, the Boussinesq model is used, where the depth-averaged eddy viscosity is computed with the *k-eps* model. The bed evolution is computed by solving the conservative law equation for sediment mass (Exner, 1920), with a closure relationship for the sediment transport rate using the Van Rijn (1984) formula, which is suitable for grain size diameters in the range between 0.2 and 2 mm. To account for non-uniform sediment distribution, the following steps are followed: (a) the sediment is subdivided into three classes; (b) the bedload transport rate is computed separately for each size class; (c) the magnitude and the direction of the bedload are corrected to account for local bed slope effects, secondary flow, and skin friction correction; (d) the Exner equation is applied for each size class of sediment and then the individual bed evolution of each class is summed to obtain the total bed evolution.

The correction of the direction of bedload transport due to bed slope follows the van Bendegom (1947) relation:

$$\tan\alpha = \frac{\sin\delta - \frac{1}{f(\theta)}\frac{\partial Z_b}{\partial y}}{\cos\delta - \frac{1}{f(\theta)}\frac{\partial Z_b}{\partial x}} \tag{2}$$

where α is the angle between the bed load direction and the x–axis (∘), δ is the angle between the flow direction and the x–axis (∘), θ is the dimensionless shear stress (−), and Z_b is the bed elevation (m). The formula of Talmon et al. (1995) accounting for the deviation of bedload is:

$$f(\theta) = \beta_2\sqrt{\theta} \tag{3}$$

where β_2(−) is an empirical coefficient to be calibrated (= 0.85 by default).

The correction of the direction of bedload transport due to secondary current effects on the flow direction is taken into account with the formula of Engelund (1974):

$$\delta = \tan^{-1}\left(\frac{v}{u}\right) - \tan^{-1}\left(\frac{A}{r_s}h\right) \tag{4}$$

where u, v are the depth-averaged components along the x–axis and y–axis (m/s), respectively; r_s is the local radius of curvature (m), A is the spiral flow coefficient (−), and h is the water depth (m). The secondary currents alpha coefficient α_{sc} is a parameter to be calibrated that allows the modification of the coefficient A and it can be chosen between 0.75 (rough bottom) to 1.0 (smooth bottom), that is, $\alpha_{sc} = 1$ then $A = 7$.

The correction of bedload transport magnitude due to bed slope proposed by Koch and Flokstra (1980) is applied to the bedload transport rate Q_b (kg/m/s) by a factor acting as a diffusive term in the bed evolution equation:

$$Q_b' = Q_b\left(1 + \beta\frac{\partial Z_b}{\partial s}\right) \tag{5}$$

where s (−) is the coordinate along the direction of the current and β (−) is an empirical factor accounting for the streamwise bed slope effect (= 1.3 by default).

By considering the component due to skin friction acting on bedload, the shear stress due to skin friction is determined as a function of the total shear stress with the relation:

$$\tau' = \mu\tau_b \tag{6}$$

where $\tau_b = 0.5\rho C_f(u^2 + v^2)$ is the total bed shear stress (Pa) and $\mu = C_f'/C_f$ is the friction factor (−), C_f is the friction coefficient due to form drag and skin friction (−), computed as:

$$C_f = 2\left[\log\left(\frac{30h}{ek_s}\right)/\kappa\right]^{-2} \tag{7}$$

where k_s is the equivalent roughness height of the bed (m), e is the base of the natural logarithm (−), and κ is the von Kármán coefficient taken equal to 0.4 (−). C_f' is the friction coefficient due only to skin friction (−), computed as:

$$C_f' = 2\left[\frac{\kappa}{\log(12h/k_s')}\right]^2 \tag{8}$$

where $k_s' = \alpha_{k_s}d_{50}$ is the roughness height (m) and α_{k_s} (−) is a parameter to be calibrated (=3.0 by default).

The influence of vegetation on hydrodynamics is considered as a friction source term in the momentum equations (Jang & Shimizu, 2007; Tsujimoto, 1999; Wu et al., 2005; Zhang et al., 2013), as follows:

$$\overrightarrow{F_d} = (F_{dx}, F_{dy}) = -0.5C_d\rho_w\alpha_v m D_v min(h_v, h)\,|\overrightarrow{u_{veg}}|\overrightarrow{u_{veg}} \tag{9}$$

where F_{dx} and F_{dy} correspond to the components of the drag forces F_d (N) along the $x-$axis and y−axis direction respectively, $C_d$is the drag coefficient (−), ρ_w is the water density (kg/m^3), α_v is a shape factor equal to 1 for rigid

cylinders (−), m is the number of stems per unit area ($number/m^2$), D_v is the stem diameter (m), h_v is the plant height. The vector $\overrightarrow{u_{veg}} = (u_{veg}, v_{veg})$ is equal to the depth-averaged flow velocity $\vec{u}$ for emergent vegetation. In the case of submerged vegetation, $\overrightarrow{u_{veg}}$ is computed according to Stone and Shen (2002) to better estimate the stem layer velocity from the depth-averaged flow velocity $\vec{u}$, as follows:

$$\overrightarrow{u_{veg}} = \eta_v \vec{u} \left(\frac{\min(h_v, h)}{h} \right)^{\frac{1}{2}} \tag{10}$$

where η_v is a dimensionless coefficient and $\eta_v = \frac{1 - D_v\sqrt{m}}{1 - \frac{\min(h_v, h)}{h} D_v\sqrt{m}}$.

The influence of vegetation on sediment transport is computed from the total flow intensity parameters Ψ_t and vegetation characteristics (Armanini & Cavedon, 2019; Bonilla-Porras et al., 2020), as follows:

$$\Psi_v = \Psi_t \left(1 + K_v \Omega_v \frac{h_v}{D_v} \right) \tag{11}$$

$$K_v = 49.38 \left(\frac{h_v}{h} \right)^{-0.92} - 10.97 \left(\frac{h_v}{h} \right)^{-1.92} \tag{12}$$

where Ψ_v is the flow intensity parameter in vegetated beds (−), and Ω_v is the plant areal density of (−). Equations 11 and 12 were derived based on the flume experiments by Armanini and Cavedon (2019), with three different vegetation density areas and one unvegetated area. Previous numerical results (see Li et al., 2020, for a complete description) show that the formulas can reproduce the abrupt changes in the bottom at the transition zone between the different density areas, similarly to the observation in Armanini and Cavedon (2019).

The biomorphodynamic model couples the hydrodynamic module TELEMAC-2D, the sediment transport and morphodynamic module GAIA and the dynamic vegetation module developed by Jourdain et al. (2020) of the open-source TELEMAC-MASCARET modeling framework (www.opentelemac.com). The solution of the hydrodynamic equations is based on the finite element method, with an edge-based N scheme for solving the advective terms in the momentum equations. The numerical scheme used for the solution of the Exner equation combines an implicit finite element discretization with an edge-based explicit upwind advection scheme (Hervouet et al., 2011). The computational domain is discretized with a finite element mesh, consisting of unstructured triangular elements.

The bank failure algorithm derives the bank slope stability factor by comparing the slope $\|\nabla \boldsymbol{n}_i\|$ of each triangular element with the bed material equilibrium slope tan φ, where $\boldsymbol{n}_i$ is the normal vector of the element i and φ is the threshold slope of stability of the material composing the riverbank. Unstable elements are considered those with an angle steeper than the angle of repose. Following Nagata et al. (2000), the threshold slope of stability is adapted to be equal to the angle of repose of the material composing the riverbank, assumed for simplicity to be identical for submerged and unsubmerged elements. For each unstable element, the bed evolution at each element node incorporates the bank failure effect as a function of the stability factor, the bed elevation at each node, the average of element node elevations, and the element area, see El kadi-Abderrezzak et al. (2016). This is equivalent to considering the rotation of an element around a horizontal axis, where a certain volume of sediment in the upper half of the element (the half which is higher than the axis) is instantaneously transported to the lower half of the element. When this step is performed, node height discontinuities are produced in nodes shared by adjacent elements. These discontinuities are then corrected by area-averaging the node height discontinuity of each element, following a procedure similar to Swartenbroekx et al. (2010).

To mimic the spatial distribution of vegetation as in the experimental tests, the condition for vegetation establishment is defined based on critical water depth h_{rec} (m): vegetation is inserted over bars if the computed water depth is smaller than the critical value (Figure 2a). Thus the critical water depth h_{rec} needs to be set and calibrated to determine the plant establishment areas. Besides, vegetation mortality due to burial (Kui & Stella, 2016) and type II uprooting (Edmaier et al., 2011) is implemented as well. However, to further calibrate the numerical model, those processes are simplified to mimic the conditions of the experiments. Plants are uprooted if bed erosion depth exceeds a critical erosion depth h_{ero} (m) which needs to be calibrated (Figure 2b). Similarly, vegetation burial occurs if deposition height exceeds a critical deposition height h_{dep} (m) which is assumed to be the same as

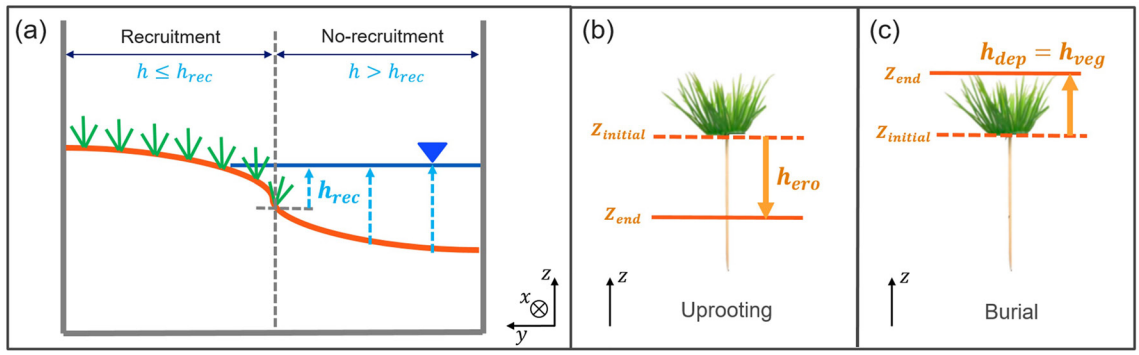

Figure 2. Modeled vegetation dynamics. (a) Establishment of vegetation: establishment areas have water depth smaller than the critical one ($h \le h_{rec}$). (b) Plant uprooting condition: local bed erosion exceeding the critical value h_{ero} to be calibrated. (c) Plant burial condition: local deposition exceeding the critical value h_{dep} assumed to be the same as the plant height.

the seedling height (Figure 2c). As in the experiments, also in the numerical model plants are added at the end of each low-flow stage, that is, every 11 hr.

To numerically represent the filled patch pattern, one critical water depth h_{rec1} (Figure 2a) is used to determine the outside patch contour of the vegetated area and the condition for the filled patch pattern formation is $h \le h_{rec1}$, see Figure 3a. Instead, two critical water depths h_{rec1} and h_{rec2} are used to delimit the outside and inside patch contour of the stripe pattern (Figure 3b). For the second case, the condition to vegetation establishment verifies $h_{rec2} \le h \le h_{rec1}$. In this work, vegetation growth is not considered, as Vargas-Luna's experiments used artificial plants.

2.3. Numerical Model Set-Up

The computational domain is equal to the full flume length (Figure 1a) of the laboratory experiments by Vargas-Luna, Duró, et al. (2019). It is discretized with an unstructured mesh composed of 136,374 nodes and 270,502 triangular elements, with an average edge length of 0.03 m. The time step is set to 0.03 s to keep the Courant number smaller than 1.0 to guarantee numerical stability. The initial channel bed is flat and set to 4.0 m elevation. The non-uniform sediment is composed of three size classes, of respectively 0.5 mm, 1 and 1.7 mm with initial fractions equal to 0.3, 0.2 and 0.5, respectively. Hydrodynamic initial conditions are determined from a numerical simulation considering a fixed bed and a constant flow discharge.

The upstream hydraulic boundary conditions correspond to a series of low and high-flow discharges (Figure 1e) and the downstream free surface elevations are set to 4.08 and 4.13 m, for low and high discharges, respectively. Sediment recirculation is implemented in the model to best represent the experimental conditions, while the sediment transport rate and the bed level at downstream boundaries are left free of conditions. The critical Shields parameter is set to 0.03, as proposed by Vargas-Luna, Duró, et al. (2019) and the angle of repose of the bank material is assumed to be equal to 40°.

Considering the plant height (only 0.03 m), the plastic material, and the diameter of the tussock, each tussock is considered as a short rigid cylinder in the numerical model and its vertical variation can be considered negligible. Due to the unavailability of measurement, the shape factor α_v and the drag coefficient C_d are assumed to be 1 by default. Sensitivity analysis on these coefficients is presented later in this study to discuss the potential impact of the drag force induced by vegetation on the main results. Accordingly, the vegetation density in Equation 9 is 112 plants per square meter, with a plant diameter of 0.022 m and a height of 0.03 m. The areal density Ω_v in Equation 11 is equal to 0.0425 based on the calculation from the diameter of the tussock. Different from the staggered pattern for plants distribution in the laboratory experiments, plants are accounted for at each node by solving Equations 9 and 11, coupled to the shallow water and sediment transport equations at each time step in the numerical model. Therefore, sediment transport processes at the stem scale are not represented in this study. This coupling is not considered when the condition for vegetation mortality is satisfied.

Numerical model calibration and validation are performed on the three scenarios of the experiments of Vargas-Luna, Duró, et al. (2019). The calibrated value of the bed roughness height k_s is 0.007 m. The calibrated values

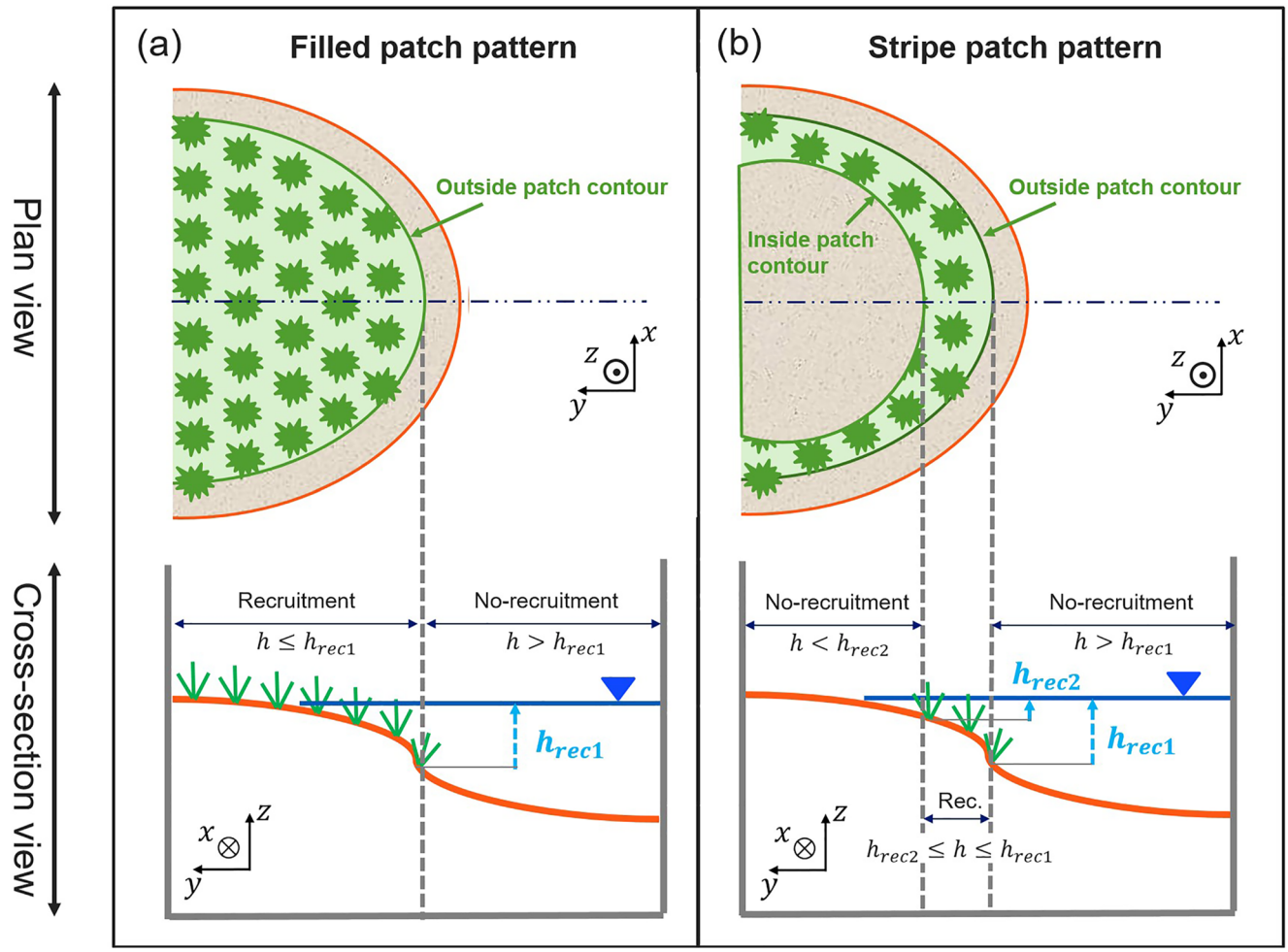

Figure 3. Vegetation establishment conditions for: (a) filled patch and (b) stripe patch patterns.

of the coefficients weighing the effects of bed slope (Equations 2 and 5), secondary flow (Equation 4) and skin friction correction (Equation 6) on sediment transport are β_2=1.6 and β = 1.3, α_{sc} = 0.95, and α_{ks} = 4.0, respectively. Finally, the calibrated value of the critical erosion depth h_{ero} is 0.035 m, corresponding to the half root length (= 0.07 m in Figure 2b). The calibrated biomorphodynamic model was then validated based on the results of Scenario (3) of Vargas-Luna, Duró, et al. (2019) with vegetation both on floodplain and emerging bar tops. More details on the calibration and validation processes are provided in Supporting Information S1.

Table 1
Model Scenarios

Scenario name	$h_{rec1}(m)$	$h_{rec2}(m)$
F-ref	0.034	-
S-ref	0.034	0.030

Note. The first letter in the scenario name indicates F = "Filled" or S = "Stripe" patterns. "Ref" suffix refers to reference scenarios.

2.4. Numerical Scenarios

This study assesses the influence of filled versus stripe vegetation patch patterns on channel biomorphodynamics. To better compare the numerical results, the imposed critical water depth h_{rec1} equals 0.034 m for both two patch patterns, resulting in the same initial outside patch contour (Figure 3). An additional critical water depth h_{rec2} of 0.03 m is set as well for the stripe pattern to form the inside patch contour (Table 1). The initial bed topography is the same for all scenarios and corresponds to the results of the calibration at 42 hr (with vegetation on both floodplains and emerging bars). The

Table 2
Sensitivity Analysis Scenarios

Critical water depth for vegetation establishment h_{rec1}	Scenario name	$h_{rec1}(m)$
	F-Srec	0.032
	S-Srec	0.032
	F-Lrec	0.038
	S-Lrec	0.038
Critical erosion depth for uprooting h_{ero}	Scenario name	$h_{ero}(m)$
	F-Sero	0.018
	S-Sero	0.018
	F-Lero	0.052
	S-Lero	0.052
Drag coefficient C_d	Scenario name	$C_d(-)$
	F-Scd	0.5
	S-Scd	0.5
	F-Lcd	1.5
	S-Lcd	1.5

Note. The first letter in the scenario name indicates F = "Filled" or S = "Stripe" patterns. The second capital letter indicates a S = "Small" or L = "Large" value for the parameters rec = "critical water depth h_{rec1}," ero = "critical erosion depth h_{ero}" and cd = "drag coefficient C_d."

boundary conditions (upstream water discharges and downstream water depths in Section 2.1) and vegetation characteristics (introduced in Section 2.3) used in both scenarios are identical.

2.5. Sensitivity Analysis Scenarios

Previous studies (Bertoldi et al., 2014; Jourdain et al., 2020) have shown that different vegetation characteristics can significantly impact the numerical results, since they can act differently on the flow field and sediment transport (Equations 9–11), and affect the long-term channel evolution. For this, 12 additional scenarios (Table 2) were carried out to include sensitivity analyses on the impact of the following vegetation coefficients: the critical water depth for vegetation establishment, h_{rec1}, to investigate the effects of the vegetated area extension; the critical erosion depth, h_{ero}, to examine the impact of uprooting resistance; and the drag coefficient, C_d, to assess the effects of the drag force induced by vegetation. The main purpose of the sensitivity analyses is to qualitatively assess the impact of variations of these coefficients on the main results of channel bed evolution compared with the reference cases of the filled pattern versus the stripe pattern.

In this work, *Srec* and *Lrec* denote a small value of h_{rec1} (0.032 m) and a large value of h_{rec1} (0.038 m), corresponding to the initial condition where bars are slightly or fully covered by vegetation, respectively. Scenarios *Sero* ($h_{ero} = 0.018$ m) and *Lero* ($h_{ero} = 0.052$ m) correspond to one-quarter and three-quarters of root length, representing small and large resistance to uprooting, respectively. Similarly, scenarios *Scd* ($C_d = 0.5$) and *Lcd* ($C_d = 1.5$) correspond to the two contrast conditions of the drag force.

3. Results

3.1. Channel Biomorphodynamics Evolution at the Reach-Scale

Plan views of bed level and spatial vegetation distribution at different simulation stages are shown in Figure 4 for the filled (F-ref) and the stripe (S-ref) patterns. The corresponding bed level changes are presented in Figure 5.

For both patch patterns, during high flows, sediment deposition mainly occurs upstream of vegetated bars, as well as along the main channel near the lateral edge of vegetated bars (e.g., Figures 5a1 and 5b1). During low flows, the sediment deposited upstream of bars is eroded and the lateral sediment deposits migrate downstream

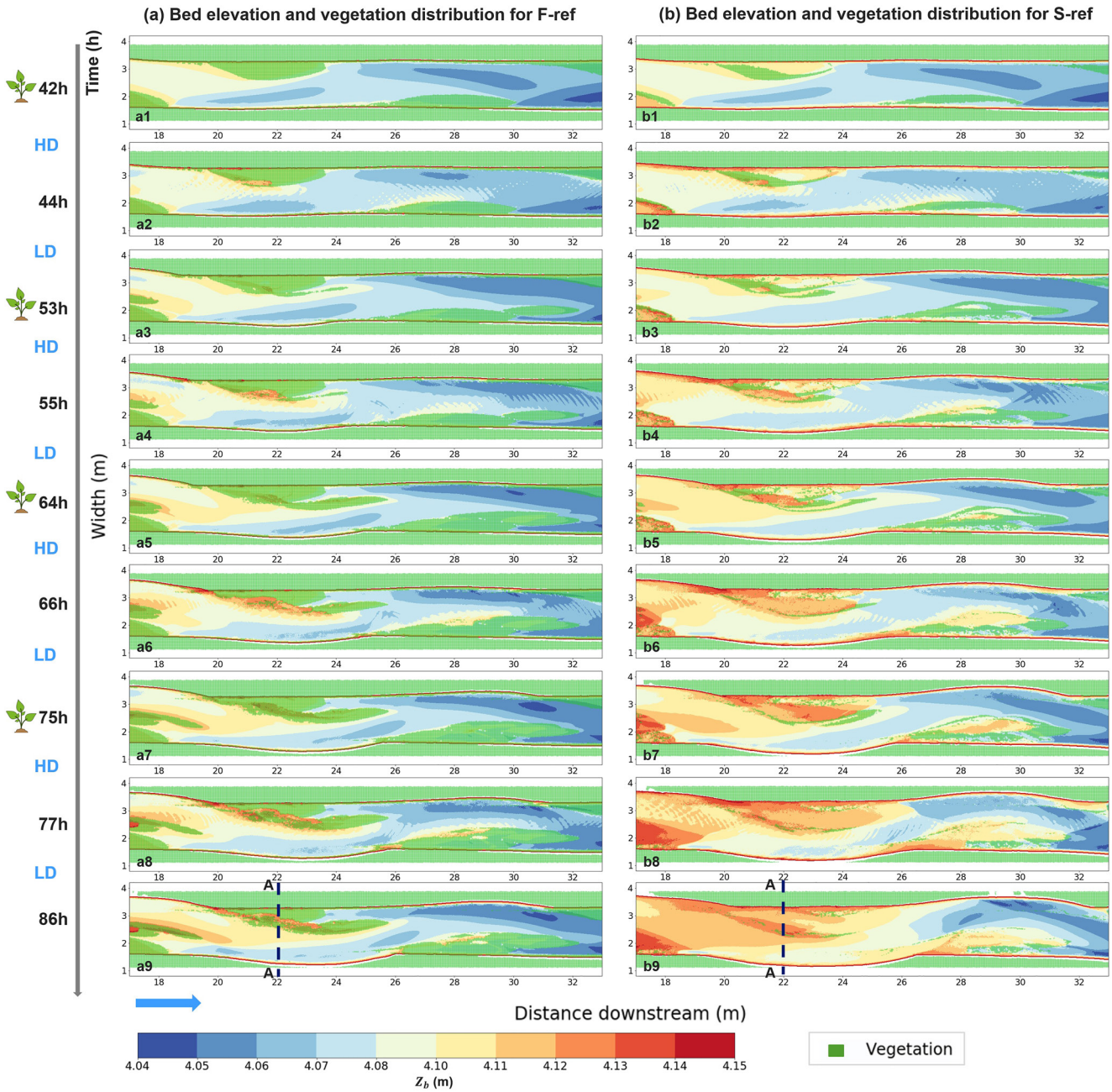

Figure 4. Computed bed elevation and vegetation distribution from 42 to 86 hr for (a) filled pattern F-ref and (b) stripe pattern S-ref. HD and LD indicate the starting moment of high- and low-flow periods, respectively. The blue arrow indicates the flow direction. Cross-section A-A is indicated with a dashed black line. The plant symbol indicates the moment of vegetation establishment update.

of vegetated bars, forming scroll bars (curvilinear ridge parallels to the channel) as shown in Figures 5a2 and 5b2. Local bank erosion occurs at the opposite side of vegetated bars, mainly at low discharge (Figure 5).

At an early stage, the distinction between sedimentation patterns during high and low flows can be explained by the different flow fields shown in Figure 6. The flow direction at high-flow stages is more uniform and parallel to the main channel, and the flow velocity within the patch decreases gradually in the downstream direction (Figures 6a and 6b). Instead, at low-flow stages, the streamlines are more sinuous and the flow follows the vegetation patch contour (Figures 6c and 6d). The highest velocities are located in the pools upstream of bars and along bar edges, where sediment was deposited during the previous high-flow stage.

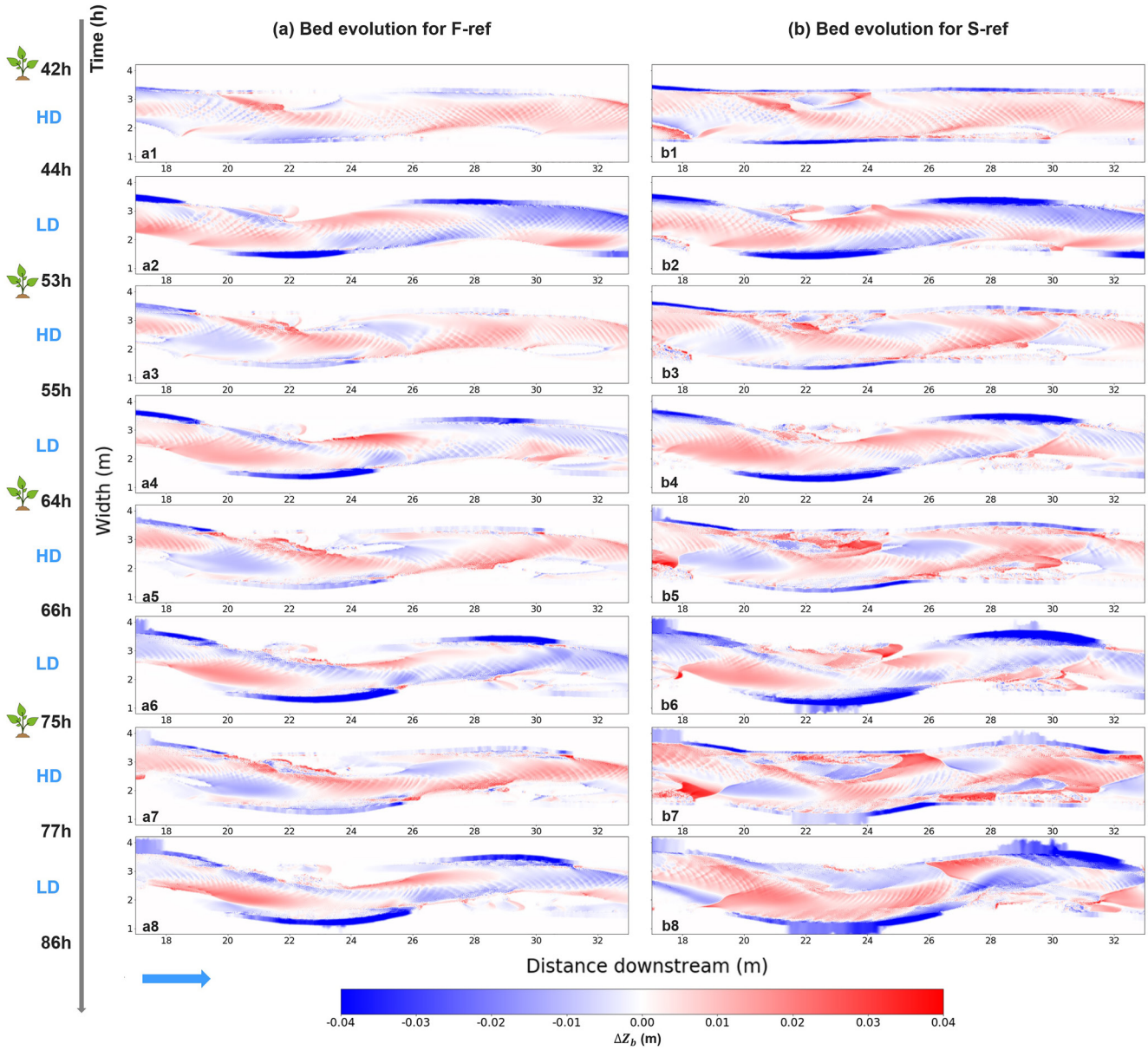

Figure 5. Computed temporal bed level changes from 42 to 86 hr for (a) the filled pattern F-ref and (b) the stripe pattern S-ref. HD and LD indicate the starting moment of high and low discharge periods, respectively. The blue arrow indicates the flow direction. The plant symbol indicates vegetation establishment update.

Due to local water depth reduction at low-flow stages, the scroll bars forming downstream of vegetated bars become suitable areas for the establishment of new vegetation (Figures 4a3 and 4b3). This impacts furthermore both local flow field and sediment transport, leading to new downstream sediment deposits, acting as a positive feedback system, which favors the growth of the scroll bars and the establishment of new vegetation, as well as the formation of chute channels. However, shorter scroll bars are found downstream, with less visible chute channels for the stripe pattern compared to the filled pattern (e.g., Figures 4a9 and 4b9) at the end of the simulation.

For both patch patterns, part of the vegetation disappears due to burial when the deposition over the vegetated bars exceeds the vegetation height (0.03 m), which occurs mainly during high flows (e.g., Figures 4a2 and 4b2). Those disappeared plants due to burial can be substituted by new plants at the next vegetation establishment moment for the filled pattern (e.g., Figures 4a2 and 4a3), but not for the stripe pattern (e.g., Figures 4b2 and 4b3), which can be explained by different vegetation establishment strategies. At the end of the simulations, the number of plants

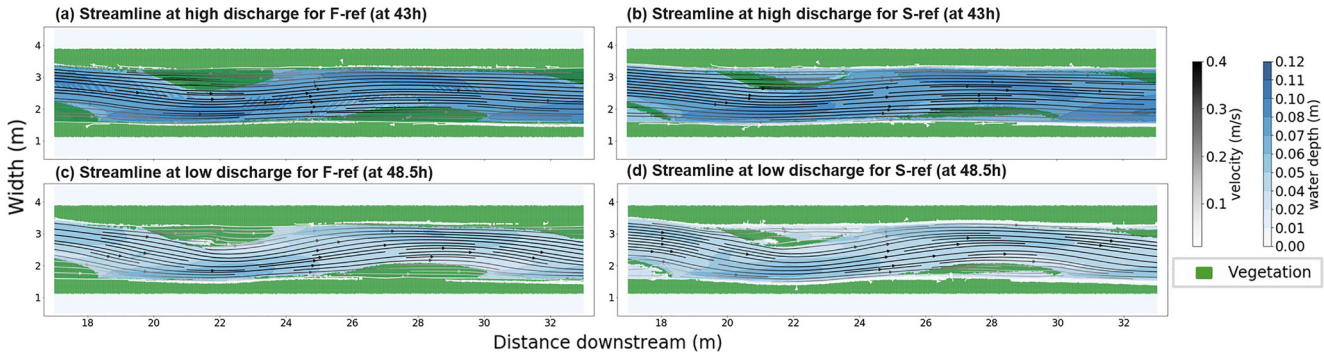

Figure 6. Streamlines during high-flow stages for (a) the filled F-ref, and (b) the stripe (S-ref) patch patterns. Streamlines during low-flow stages for (c) the filled and (d) the stripe patterns.

increased by 20% with the filled pattern, whereas it decreased by 23% with the stripe pattern (more details can be found in Supporting Information S1). Nonetheless, the bar elongation rates remain similar in the two scenarios.

Differences between the two scenarios are more remarkable at the reach-scale. Figure 7 describes the temporal evolution of the reach-averaged channel characteristics for scenarios F-ref and S-ref, starting from 42 to 86 hr. Averaging of channel width, water depth and slope along the thalweg is carried out for the reach between $x = 17$ and 33 m. For both scenarios, the main channel tends to be wider, shallower and steeper as time passes (Figure 7). This behavior is more relevant for the stripe pattern than for the filled pattern. At the end of the simulation, the average channel width is 2.20 m for the stripe pattern, 5.6% larger than the 2.08 m obtained with the filled pattern. Furthermore, for the filled (stripe) pattern, the water depth is 0.039 m (0.036 m), the slope 0.0025 (0.0033), and the time-averaged sediment transport rate at the outflow 44.5 kg/hr (50.40 kg/hr). The sediment transport rates show that more sediment exits the channel with the stripe pattern configuration at low flows, the opposite is observed at high flows.

3.2. Flow, Sediment and Vegetation Processes at the Cross-Sectional Scale

To better understand the interactions between flow, sediment and vegetation dynamics, the transversal distribution of the sediment transport rates, bed and water levels and vegetation cover is depicted in Figure 8 for the period between 42 and 86 hr (cross-section A-A location is indicated in Figure 4).

For both the filled and the stripe patch patterns, the sediment transport rate decreases drastically from the non-vegetated main channel to the lateral edge of vegetation. During the first high-flow period, from 42 to 44 hr, sediment is deposited mainly near the edge of the vegetated area (between $x = 2.4$ to $x = 2.6$ m, Figures 8a and 8b). Bank erosion opposite the vegetated bar is observed for both scenarios, but it is reduced for the filled pattern due to bank protection by vegetation. Besides, the bare area within the stripe patch is slightly eroded.

During the low-flow stage, from 44 to 53 hr, sediment deposits are found mainly within the vegetation patch and in the main channel, while the sediment deposited along the patch border during the former high-discharge stage is eroded (compare Figures 8b and 8c). The bed level at 53 hr obtained with the stripe pattern scenario is only slightly higher (approximately 0.005 m) in comparison to the filled pattern scenario. Under the condition that water depths are smaller for the stripe pattern (due to larger bank erosion leading to a larger channel), the newly established vegetation in the stripe pattern scenario shows a larger lateral extension (to $x = 2.52$ m) than in the filled pattern scenario ($x = 2.46$ m).

During the high-flow stage (from 53 to 55 hr), new sediment is deposited at the edge of the vegetated bars resulting in local vegetation burial (between $x = 2.2$ and 2.37 m, Figures 8c and 8d), for both patch patterns. Nevertheless, traces of vegetation are still observed nearby the vegetated patch. The width of this vegetated area is about 0.14 m for the stripe pattern, which is much larger than the one for the filled pattern (0.01 m). At the same location, the bed level increases for the stripe pattern (around +0.005 m), but is eroded for the filled pattern (around −0.012 m) during the next low-flow period (from 55 to 64 hr, Figures 8d and 8e). This allows newly added vegetation at 64 hr to expand laterally until $x = 2.61$ m for the stripe pattern. While for the filled pattern, the vegetation

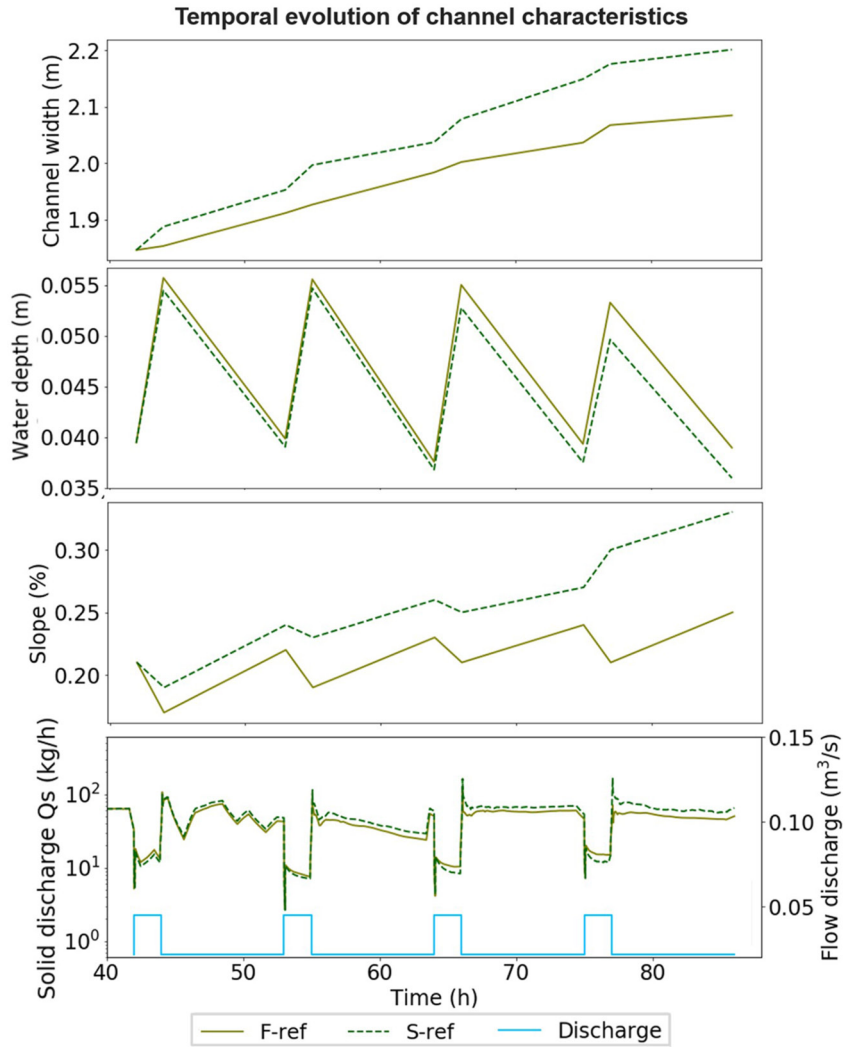

Figure 7. Temporal evolution of reach-averaged channel width, water depth, bed level slope along the thalweg, solid discharge at the flume with the indication of water discharge.

remains fixed at approximately $x = 2.45$ m. Vegetation mortality due to burial occurs again during the following high-flow stage (Figure 8f) and during the next low-flow stage, vegetation expands laterally to $x = 2.7$ m for the stripe pattern, but no expansion occurs for the filled pattern (Figure 8g). Following the outermost plant location, sediment is deposited during the next high discharge around $x = 2.43$ m and $x = 2.7$ m for the filled and the stripe pattern, respectively (Figure 8h). Meanwhile, the bed is eroded within the stripe patch ($x = 1.98$–2.4 m) due to a lack of vegetation, and deposition is found at $x = 1.77$–1.93 m from the collapsed left bank for the stripe pattern.

Figure 9 presents the bed level profiles of Cross-section A-A (location shown in Figure 4) for the two patch patterns. For the filled pattern (Figure 9a), the vegetated area near the left bank can be divided into two parts: the edge ($x = 2.0$–2.5 m) and the inner area ($x < 2.0$ m). Bed level increased in the edge area, whereas there is no sediment input to the inner part. Bed level rises also in the main channel. This is related to slope increase that results in dominance of deposition in the upstream part of the channel and dominance of bed erosion in the downstream part which is visible in Figure 4. Note that Cross-section A-A is located in the upstream half of the channel. Compared to the filled pattern, the stripe pattern shows a slightly larger cross-section with slightly higher bank erosion mainly occurring at the right side of the channel. After 75 hr, some bed erosion occurs also at the left bank toe, slightly increasing the bank instability leading to some bank retreat also at the left side of the channel (Figure 9b). The final configuration shows some bed level rise at the toe of both eroding banks, which is

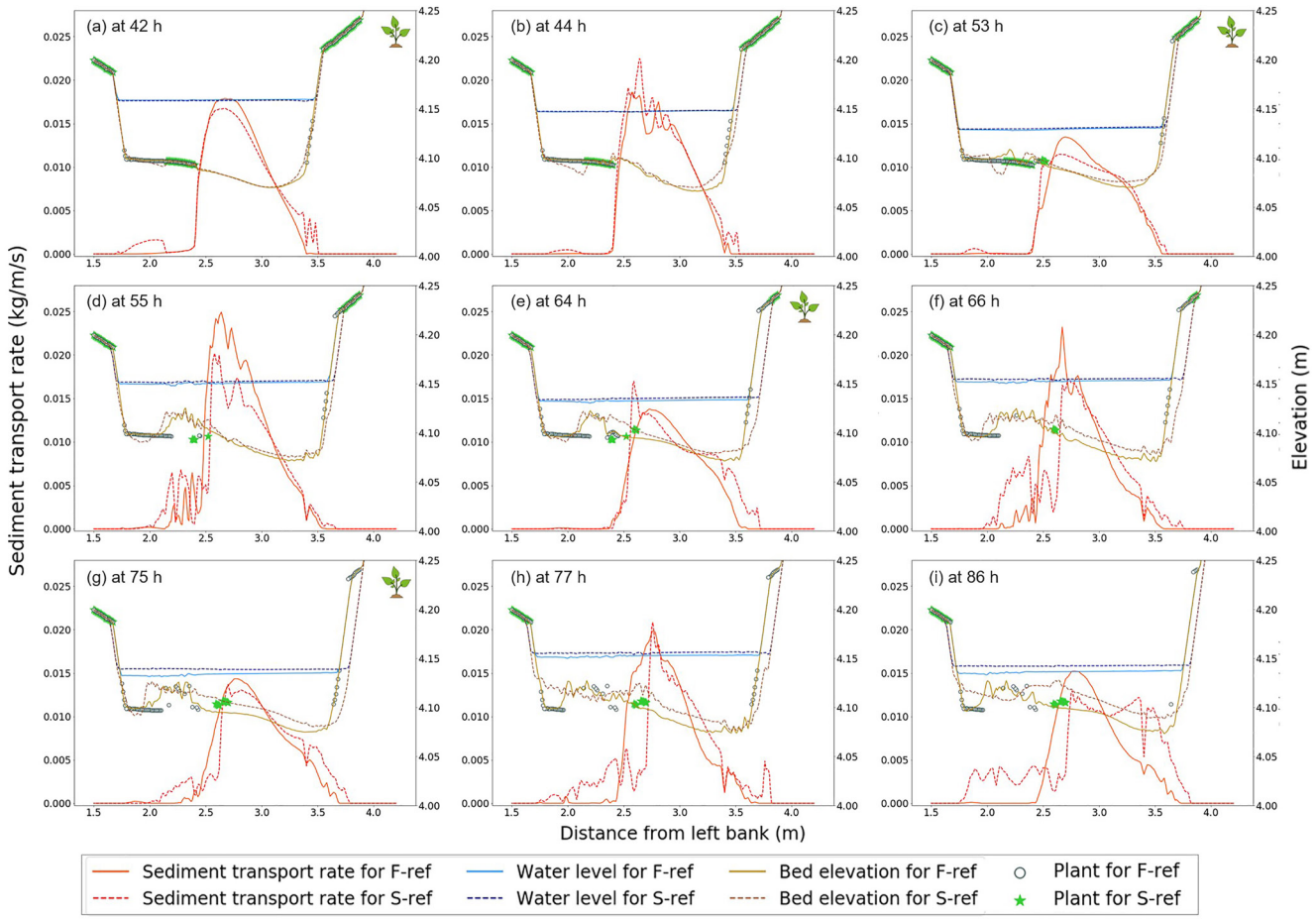

Figure 8. Sediment transport rate, water level, bed elevation, and vegetation obtained for the two scenarios at Cross-section A-A (Figure 4) at different times from 42 to 86 hr. The plant symbol indicates the vegetation establishment updates. View from upstream.

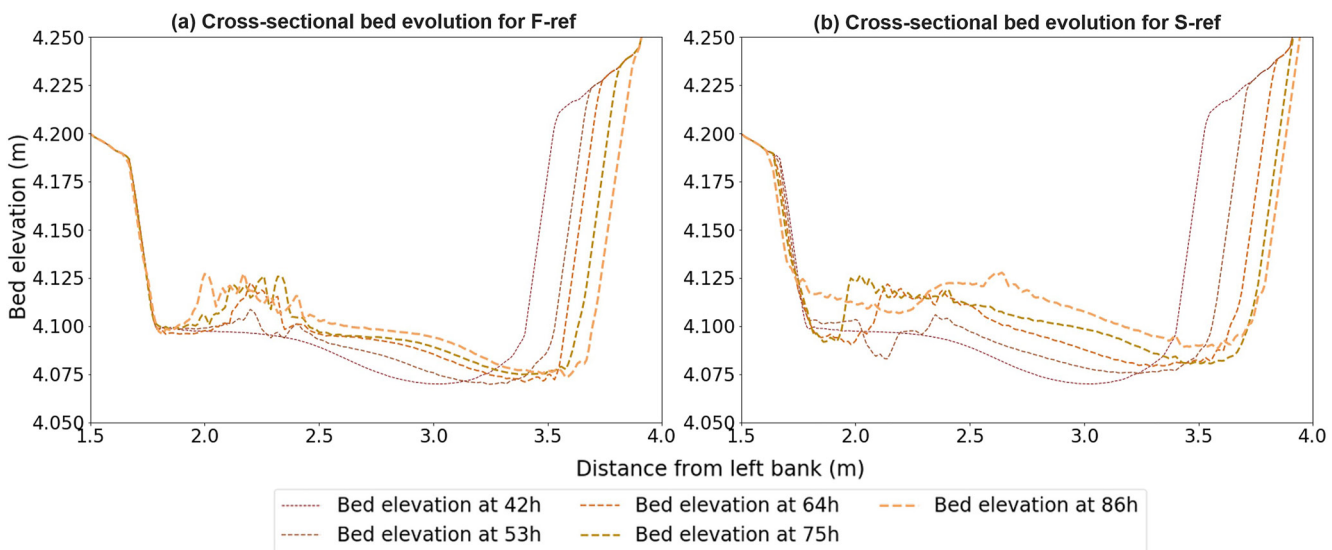

Figure 9. Bed level profiles of Cross-section A-A at different times (Figure 4) for (a) the filled patch pattern and (b) the stripe pattern. View from upstream.

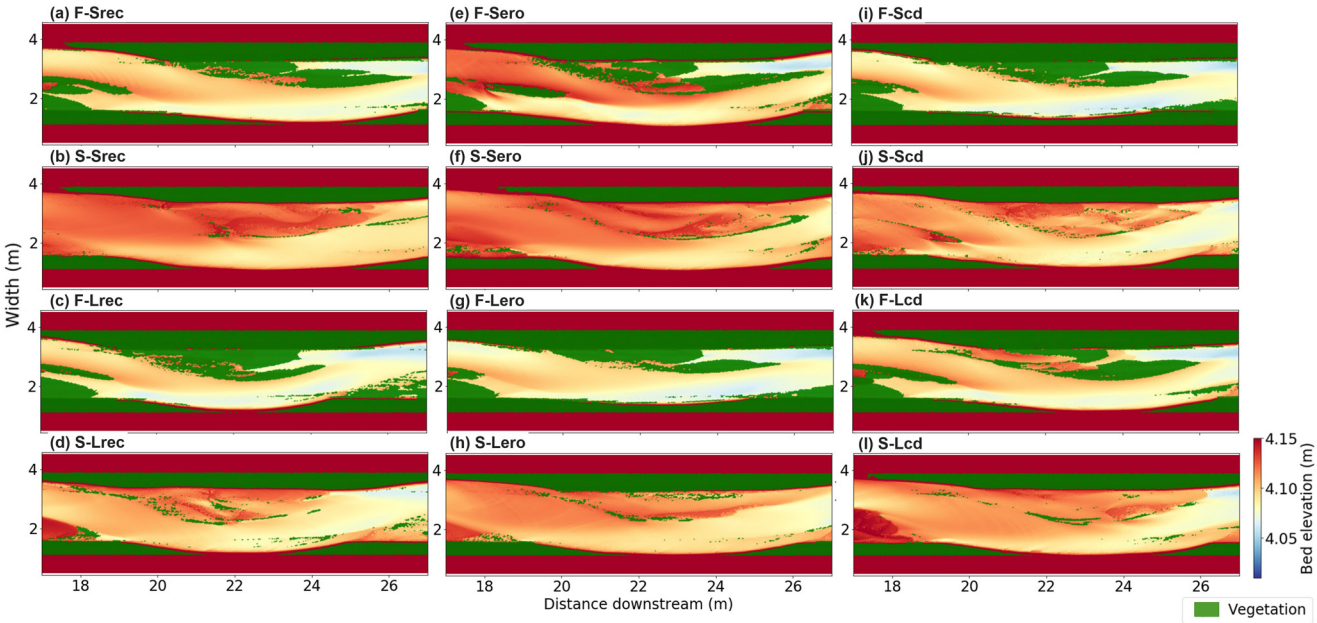

Figure 10. Bed level and vegetation distribution at the end of the computations.

due to the accumulation of bank material. The newly added vegetation in the stripe pattern tends to expand laterally toward the main channel so that the highest part of the bed gradually moves toward the middle of the channel.

3.3. Sensitivity Analysis

To consider and justify the impact of different vegetation coefficients on the numerical results, 12 sensitivity analysis scenarios were computed on: the critical water depth h_{rec1}, the critical erosion depth h_{ero}, and the drag coefficient C_d (introduction in Section 2.6). Figure 10 presents the final bed level and vegetation distribution over the bar from $x = 17$–27 m and Table 3 presents reach-averaged channel characteristics including channel width, water depth, bed level slope derived from the thalweg, and solid discharge at the exit of the flume at 86 hr.

For the critical water depth h_{rec1} describing vegetation establishment area, results show that a smaller value of h_{rec1} (F-Srec and S-Srec) presents longer bars (bar length approx. 6 m, see Figures 10a and 10b) which elongate

Table 3
Reach-Averaged Channel Characteristics for Sensitivity Analysis Scenarios After 86 hr

	Scenario name	Channel width (m)	Water depth (m)	Slope (%)	Temporal averaged solid discharge (kg/h)
Critical water depth for vegetation establishment h_{rec1}	F-Srec	2.13	0.038	0.29	47.7
	S-Srec	2.28	0.034	0.29	54.2
	F-Lrec	2.06	0.039	0.26	43.8
	S-Lrec	2.13	0.035	0.30	45.6
Critical erosion depth for uprooting h_{ero}	F-Sero	2.26	0.036	0.39	55.4
	S-Sero	2.31	0.034	0.30	55.0
	F-Lero	1.95	0.04	0.20	42.0
	S-Lero	2.18	0.034	0.31	49.5
Drag coefficient C_d	F-Scd	2.01	0.039	0.22	41.2
	S-Scd	2.18	0.034	0.36	48.8
	F-Lcd	2.13	0.038	0.30	48.0
	S-Lcd	2.21	0.034	0.32	49.8

faster, compared to a larger value (F-Lrec and S-Lrec) (bar length approx. 4 m, see Figures 10c and 10d). At the final stage, the channels forming for scenarios Srec are larger, shallower and steeper with more sediments leaving the flume, compared to the scenarios Lrec (Table 3). These results suggest that a smaller critical water depth h_{rec1} corresponding to a smaller outside patch contour on bars (see in Figure 3) leads to a faster bar elongation rate, thus a longer scroll bar, chute channel and larger bank erosion area, in contrast with a larger value of h_{rec1}.

Similarly, for the criterion of uprooting h_{ero}, the difference in channel morphology between the filled and stripe patterns under a smaller critical erosion depth h_{ero} (F-Sero and S-Sero) is relatively less marked, compared to the scenarios with a larger h_{ero} (F-Lero and S-Lero), see Figures 10e–10h. In particular, for the channel width (Table 3), F-Sero and S-Sero present similar channel widths by a difference of 0.002 m, which is 0.006 m for F-Lero and S-Lero. This can be explained by the results found in the previous sub-section 3.1, in which vegetation uprooting occurs mainly on the banks and only scarcely on the bars. Due to the different vegetation establishment conditions for the two patterns, there is less vegetation on the banks for the stripe pattern than in the filled pattern. Therefore, bank erosion occurs more easily with the stripe pattern than with the filled pattern (see F-ref and S-ref in sub-Section 3.2). However, this difference becomes less significant with a smaller critical erosion depth h_{ero}, indicating the case in which vegetation can be easily uprooted.

For the drag force induced by vegetation represented through the drag coefficient C_d, the results show that for both the filled and stripe patterns, the bar dynamics (location, bar length) are only weakly impacted by this coefficient (Figures 10i–10l), in comparison to the previous sensitivity tests. However, bank erosion processes due to flow deflection caused by vegetation on bars are still impacted by this coefficient. Due to the few vegetation located on bars in the stripe pattern, the final channel widths (S-Scd and S-Lcd) present only a slight difference of 0.027 m (Table 3). Conversely, for the filled pattern, a larger C_d corresponding to a higher drag force leads to stronger bank erosion and larger channel width (F-Scd and F-Lcd in Table 3).

4. Discussion

Numerical results obtained with two different patch patterns confirm the results of previous studies, demonstrating that the vegetation established on the bars can increase the flow deflection toward the opposite bank causing localized bank erosion (Bennett et al., 2008; Rominger et al., 2010; Vargas-Luna, Duró, et al., 2019). Nevertheless, the bank erosion rates are found higher with the stripe pattern than with the filled pattern, which can be explained by the fact that the filled pattern presents more vegetation on banks than the stripe pattern (Figure 8).

Final channels (Figures 4a9 and 4b9) exhibit a tendency to develop an anabranch system with both patch patterns, with a gradual development from alternate bars to central bars. This corresponds to the evolution observed in the experiments of Vargas-Luna, Duró, et al. (2019), which is due to increased bar mode resulting from the increased width-to-depth ratio. However, the central bar top with the stripe pattern is located closer to the channel centerline than the one with the filled pattern, due to a larger width-to-depth ratio.

Scroll bars develop downstream of vegetated bars with both patch patterns, with the form of a curvilinear ridge more or less parallel to the channel. These scroll bars become suitable areas for new vegetation colonization (Figure 4), which is consistent with the numerical findings of Jourdain et al. (2020) on the morphodynamics of vegetated alternate bars on a simplified reach of the Isère River in France. *In situ* observations by Corenblit et al. (2016) on the *P. nigra* colonized on two point bars along the channelized Garonne River in France demonstrate that upstream pioneer cohorts facilitate new vegetation establishment downstream of the point bar.

Vegetated scroll bars contribute to chute channel formation and elongation between the most upstream bar and the channel bank. Nevertheless, in the end, the chute channels with the stripe pattern are shorter and less pronounced, compared with the ones with the filled pattern (Figure 4). Two possible explanations are:

1. Due to the different vegetation establishment strategies and the morphological evolution during the first 11 hr, the newly vegetated areas established on the scroll bars are relatively shorter with the stripe pattern compared to the filled pattern (Figures 4a3 and 4b3). Subsequently, the non-vegetated areas tend to be eroded during the next high-flow period (Figures 4a4 and 4b4);
2. Unlike the filled pattern, in which sediment transport is negligible within the vegetation patch, sediment transport is maintained within the stripe patch because of the specific non-vegetated "hollow" structure (Figure 4). Sediments are therefore transported downstream and fill the chute channels.

A part of vegetation mortality on bars is observed for both patterns. In the simulations, mortality occurs mainly due to burial at the lateral edge of the vegetation patch during the high-flow period. The establishment condition for the filled pattern allows vegetation to recover on bars quickly, whereas this is not the case for the stripe pattern. Therefore, the final vegetation coverage on bars is significantly less with the stripe pattern than with the filled pattern (Figure 4). However, surprisingly, bar elongation rates for both patch patterns are similar, despite the fact that the stripe pattern presents a situation close to the non-vegetated bar condition with only a few plants forming a curved contour line. For both patch patterns, the sediment transport rates and the flow velocity are strongly reduced at the outermost plant location, from the main channel toward the inside of the vegetation patch (Figure 8), in agreement with the experimental observations by Bennett et al. (2002) and Rominger et al. (2010). These findings suggest that the frontal projected area of the vegetation patch in the streamwise direction (further explanation in the supporting material) can significantly influence the bar dynamics, while the average vegetation density within the patch appears to be less impacting.

With the stripe pattern, the final channel is larger, shallower, and steeper with a higher sediment transport rate than with the filled pattern (Figure 7). By analyzing the biomorphodynamic interactions in chronological order at the cross-section scale, it appears that the differences in bank erodibility due to the different plant locations on banks are the initial triggers for deviating the morphological evolution. This hypothesis can be supported by the results of the sensitivity analysis on the parameter of the critical erosion depth (Figures 10e–10h). The distinction of channel evolution between two patterns is reduced if plants are more easily uprooted (i.e., with a smaller critical erosion depth for uprooting h_{ero}), corresponding to the condition in which the two patterns have more similar vegetation characteristics on banks resulting in more similar bank erodibility. Besides, the sensitivity analysis shows that the critical water depth for vegetation establishment h_{rec1} (Figures 10a–10d) can have an influence on the vegetated bar elongation rates. The drag force induced by vegetation on water flow (tested by modifying the drag coefficient C_d) seems to only have an impact on the filled pattern by affecting flow deflection, but has a very limited impact on the stripe pattern with only a few aligned plants present on bars (Figures 10i–10l). However, the differences between the two patch patterns in vegetation coverage and chute channel formation are not impacted by these three coefficients above.

Limitations arising from the modeling hypotheses need to be mentioned. The study focuses on the channel morphodynamic evolution with different vegetation patch patterns at the reach-scale. Therefore, the stem-scale eddies due to individual plants are not considered. Their effects are accounted for as extra energy dissipation through the value of the roughness coefficient. The numerical model presented in this study is built, calibrated and validated on the laboratory experiments of Vargas-Luna, Duró, et al. (2019), which were inspired by field observations on a small stream located in the Netherlands. Therefore, the results presented in our study could be upscaled to small-scale streams in which the effects of vegetation on morphodynamics have a large influence. To reproduce the artificial grass used in the laboratory experiments, in which vegetation growth is not considered, the vegetation dynamics included in the model are also simplified. Therefore, applications of this model to the long-term evolution of large-scale rivers should include a proper description of vegetation dynamics. Drag force variations induced by vegetation growth could impact the presented results, which can be confirmed by the sensitivity analysis performed on the drag coefficient C_d. The experiments of Kui and Stella (2016) on long-term survival following complete burial for seedlings and saplings show that not all plants are killed by complete burial, suggesting that the vegetation mortality set up in our model should not be applied to certain plant species. Due to specific boundary conditions, in this study vegetation mainly dies due to burial. However, several studies (e.g., Bau et al., 2021; Caponi & Siviglia, 2018) point out the importance of belowground vegetation in impacting river morphodynamics. This suggests that a root distribution model should be further considered, as well as a physical-based uprooting mechanism for more realistic study cases.

5. Conclusions

The present study aimed at investigating the influence of two realistic vegetation patch patterns, namely defined as filled and stripe patterns, on channel morphodynamics with alluvial bars. A two-dimensional numerical biomorphodynamic model was developed and validated against laboratory experiments with vegetation establishment on floodplain and emergent alternate bar tops. To form the two patch patterns in the numerical model, different critical water depths were applied to simulate the distinct vegetation establishment conditions. Vegetation mortality due to burial and uprooting was modeled by respectively setting a critical deposition height and an

erosion depth. Fourteen scenarios have been simulated, including scenarios of sensitivity analysis on vegetation coefficients, that is, critical water depth for vegetation establishment, critical erosion depth for vegetation uprooting, and drag coefficient for drag force.

Numerical results show that the channel morphological responses to two different vegetation patch patterns have similarities and differences. Both vegetation patch patterns on bars reduce the flow velocity (as well the sediment transport rate) near and within the patch, pushing the flow toward the opposite bank and causing localized bank erosion. In addition, they both similarly influence the bar elongation rates, presenting scroll bars downstream and chute channels formation, despite significantly less vegetation coverage on bars with the stripe pattern. However, the scroll bars forming with the stripe pattern are shorter and less visible due to different vegetation establishment conditions. At reach-scale, the final channel configurations obtained with the two patch patterns result in a larger, shallower and steeper channel, with alternate bars transforming toward central bars. Nevertheless, these morphological responses with the filled pattern are weaker compared to the ones with the stripe pattern.

This study provides new insights into the importance of considering spatial vegetation distribution (especially the frontal projected area of the vegetation patch in the streamwise direction, see supporting information) for the morphological evolution of fluvial systems at the bar scale. Numerical results suggest that reducing the frontal projected area of the vegetation patch could be an efficient solution to remobilize river bars. This finding can help river managers to conceive effective scenarios for restoration plans. The authors have observed, for example, that the vegetation removal operation performed on the Isère River in France consists in cutting most vegetation over bars but keeping the plants aligned along the bar contour near the channel, creating patches that are similar to the stripe pattern. However, numerical simulations showed that this operation would be ineffective to remobilize river bars.

Data Availability Statement

The authors gratefully acknowledge the support of Electricité de France (EDF), Prof. A. Armanini and J.A. Bonilla Porras (University of Trento) for their formula of bedload through vegetation (https://doi.org/10.1016/j.advwatres.2021.103928) and for sharing experimental data to validate the implementation.

Acknowledgments
The authors also thank the Reviewers and Editors for their high quality and constructive reviews of our manuscript. The experimental data of Vargas-Luna, Duró, et al. (2019) are available online (https://doi.org/10.6084/m9.figshare.7591643).

References

Abderrezzak, K. E. K., Moran, A. D., Tassi, P., Ata, R., & Hervouet, J. M. (2016). Modelling river bank erosion using a 2D depth-averaged numerical model of flow and non-cohesive, non-uniform sediment transport. *Advances in Water Resources*, *93*, 75–88. https://doi.org/10.1016/j.advwatres.2015.11.004

Armanini, A., & Cavedon, V. (2019). Bed-load through emergent vegetation. *Advances in Water Resources*, *129*, 250–259. https://doi.org/10.1016/j.advwatres.2019.05.021

Baptist, M. J. (2005). *Modelling floodplain biogeomorphology*. Doctoral dissertation. Delft University of Technology. Retrieved from http://resolver.tudelft.nl/uuid:b2739720-e2f6-40e2-b55f-1560f434cbee. ISBN 90-407-2582-9.

Bau', V., Borthwick, A. G., & Perona, P. (2021). Plant roots steer resilience to perturbation of river floodplains. *Geophysical Research Letters*, *48*(9), e2021GL092388. https://doi.org/10.1029/2021GL092388

Bendegom, L. V. (1947). Some considerations on river morphology and river improvement. *De Ingenieur*, *59*(4), b1–b11. (Dutch. English translation: Nat. Res. Council of Canada, Technical Translation 1054, 1963).

Bennett, S. J., Pirim, T., & Barkdoll, B. D. (2002). Using simulated emergent vegetation to alter stream flow direction within a straight experimental channel. *Geomorphology*, *44*(1–2), 115–126. https://doi.org/10.1016/S0169-555X(01)00148-9

Bennett, S. J., Wu, W., Alonso, C. V., & Wang, S. S. (2008). Modeling fluvial response to in-stream woody vegetation: Implications for stream corridor restoration. *Earth Surface Processes and Landforms: The Journal of the British Geomorphological Research Group*, *33*(6), 890–909. https://doi.org/10.1002/esp.1581

Bertoldi, W., Siviglia, A., Tettamanti, S., Toffolon, M., Vetsch, D., & Francalanci, S. (2014). Modeling vegetation controls on fluvial morphological trajectories. *Geophysical Research Letters*, *41*(20), 7167–7175. https://doi.org/10.1002/2014GL061666

Bertoldi, W., Welber, M., Gurnell, A. M., Mao, L., Comiti, F., & Tal, M. (2015). Physical modelling of the combined effect of vegetation and wood on river morphology. *Geomorphology*, *246*, 178–187. https://doi.org/10.1016/j.geomorph.2015.05.038

Bonilla-Porras, J. A., Armanini, A., & Crosato, A. (2020). Sediment transport through submerged vegetation. In *River flow 2020* (pp. 1582–1588). CRC Press. Retrieved from https://www.taylorfrancis.com/chapters/edit/10.1201/b22619-220/sediment-transport-submerged-vegetation-bonilla-porras-armanini-crosato

Bonilla-Porras, J. A., Armanini, A., & Crosato, A. (2021). Extended Einstein's parameters to include vegetation in existing bedload predictors. *Advances in Water Resources*, *152*, 103928. https://doi.org/10.1016/j.advwatres.2021.103928

Bouma, T. J., Van Duren, L. A., Temmerman, S., Claverie, T., Blanco-Garcia, A., Ysebaert, T., & Herman, P. M. J. (2007). Spatial flow and sedimentation patterns within patches of epibenthic structures: Combining field, flume and modelling experiments. *Continental Shelf Research*, *27*(8), 1020–1045. https://doi.org/10.1016/j.csr.2005.12.019

Bywater-Reyes, S., Diehl, R. M., & Wilcox, A. C. (2018). The influence of a vegetated bar on channel-bend flow dynamics. *Earth Surface Dynamics*, *6*(2), 487–503. https://doi.org/10.5194/esurf-6-487-2018

Bywater-Reyes, S., Wilcox, A. C., Stella, J. C., & Lightbody, A. F. (2015). Flow and scour constraints on uprooting of pioneer woody seedlings. *Water Resources Research*, *51*(11), 9190–9206. https://doi.org/10.1002/2014WR016641

Camporeale, C., Perucca, E., Ridolfi, L., & Gurnell, A. M. (2013). Modeling the interactions between river morphodynamics and riparian vegetation. *Reviews of Geophysics*, *51*(3), 379–414. https://doi.org/10.1002/rog.20014

Caponi, F., Koch, A., Bertoldi, W., Vetsch, D. F., & Siviglia, A. (2019). When does vegetation establish on gravel bars? Observations and modeling in the Alpine Rhine river. *Frontiers in Environmental Science*, *7*, 124. https://doi.org/10.3389/fenvs.2019.00124

Caponi, F., & Siviglia, A. (2018). Numerical modeling of plant root controls on gravel bed river morphodynamics. *Geophysical Research Letters*, *45*(17), 9013–9023. https://doi.org/10.1029/2018GL078696

Corenblit, D., Steiger, J., Charrier, G., Darrozes, J., Garófano-Gómez, V., Garreau, A., et al. (2016). Populus nigra L. establishment and fluvial landform construction: Biogeomorphic dynamics within a channelized river. *Earth Surface Processes and Landforms*, *41*(9), 1276–1292. https://doi.org/10.1002/esp.3954

Corenblit, D., Vautier, F., González, E., & Steiger, J. (2020). Formation and dynamics of vegetated fluvial landforms follow the biogeomorphological succession model in a channelized river. *Earth Surface Processes and Landforms*, *45*(9), 2020–2035. https://doi.org/10.1002/esp.4863

de Saint-Venant, A. B. (1871). Théorie du mouvement non permanent des eaux, avec application aux crues des rivières et à l'introduction des marées dans leurs lits. *Comptes Rendus des séances de l'Académie des Sciences*, *73*, 237–240.

Džubáková, K., Molnar, P., Schindler, K., & Trizna, M. (2015). Monitoring of riparian vegetation response to flood disturbances using terrestrial photography. *Hydrology and Earth System Sciences*, *19*(1), 195–208. https://doi.org/10.5194/hess-19-195-2015

Edmaier, K., Burlando, P., & Perona, P. (2011). Mechanisms of vegetation uprooting by flow in alluvial non-cohesive sediment. *Hydrology and Earth System Sciences*, *15*(5), 1615–1627. https://doi.org/10.5194/hess-15-1615-2011

Engelund, F. (1974). Flow and bed topography in channel bends. *Journal of the Hydraulics Division*, *100*(11), 1631–1648. https://doi.org/10.1061/JYCEAJ.0004109

Euler, T., Zemke, J., Rodrigues, S., & Herget, J. (2014). Influence of inclination and permeability of solitary woody riparian plants on local hydraulic and sedimentary processes. *Hydrological Processes*, *28*(3), 1358–1371. https://doi.org/10.1002/hyp.9655

Exner, F. M. (1920). Zur physik der dünen. *Hölder*.

Follett, E. M., & Nepf, H. M. (2012). Sediment patterns near a model patch of reedy emergent vegetation. *Geomorphology*, *179*, 141–151. https://doi.org/10.1016/j.geomorph.2012.08.006

Guan, M., & Liang, Q. (2017). A two-dimensional hydro-morphological model for river hydraulics and morphology with vegetation. *Environmental Modelling & Software*, *88*, 10–21. https://doi.org/10.1016/j.envsoft.2016.11.008

Gurnell, A. M. (2014). Plants as river system engineers. *Earth Surface Processes and Landforms*, *39*(1), 4–25. https://doi.org/10.1002/esp.3397

Gurnell, A. M., & Bertoldi, W. (2020). Extending the conceptual model of river island development to incorporate different tree species and environmental conditions. *River Research and Applications*, *36*(8), 1730–1747. https://doi.org/10.1002/rra.3691

Hervouet, J. M. (2007). *Hydrodynamics of free surface flows: Modelling with the finite element method* (Vol. 360). Wiley.

Hervouet, J. M., Razafindrakoto, E., & Villaret, C. (2011). Dealing with dry zones in free surface flows: A new class of advection schemes. In *Proceedings of the 34th world congress of the international association for hydro-environment research and engineering: 33rd hydrology and water Resources symposium and 10th conference on hydraulics in water engineering* (p. 4103). Engineers.

Hickin, E. J. (1984). Vegetation and river channel dynamics. *Canadian Geographer/Le Géographe canadien*, *28*(2), 111–126. https://doi.org/10.1111/j.1541-0064.1984.tb00779.x

Jang, C. L., & Shimizu, Y. (2007). Vegetation effects on the morphological behavior of alluvial channels. *Journal of Hydraulic Research*, *45*(6), 763–772. https://doi.org/10.1080/00221686.2007.9521814

Johnson, W. (2000). CTree recruitment and survival in rivers: Influence of hydrological processes. *Hydrological Processes*, *14*(16–17), 3051–3074. https://doi.org/10.1002/1099-1085(200011/12)14:16/17%3C3051::AID-HYP134%3E3.0.CO;2-1

Jones, C. G., Lawton, J. H., & Shachak, M. (1997). Positive and negative effects of organisms as physical ecosystem engineers. *Ecology*, *78*(7), 1946–1957. https://doi.org/10.1890/0012-9658(1997)078[1946:PANEOO]2.0.CO;2

Jourdain, C., Claude, N., Tassi, P., Cordier, F., & Antoine, G. (2020). Morphodynamics of alternate bars in the presence of riparian vegetation. *Earth Surface Processes and Landforms*, *45*(5), 1100–1122. https://doi.org/10.1002/esp.4776

Khosronejad, A., Kang, S., & Sotiropoulos, F. (2012). Experimental and computational investigation of local scour around bridge piers. *Advances in Water Resources*, *37*, 73–85. https://doi.org/10.1016/j.advwatres.2011.09.013

Kim, H. S., Kimura, I., & Shimizu, Y. (2015). Bed morphological changes around a finite patch of vegetation. *Earth Surface Processes and Landforms*, *40*(3), 375–388. https://doi.org/10.1002/esp.3639

Kim, H. S., Kimura, I., & Shimizu, Y. (2019). Experiment and computation of morphological response to a vegetation patch in open-channel flows with erodible banks. *Water*, *11*(11), 2255. https://doi.org/10.3390/w11112255

Koch, F. G., & Flokstra, C. (1980). Bed level computations for curved alluvial channels: Prepared for the 19th IAHR Congress, New Delhi, India, February 1981. *Waterloopkundig Laboratorium*.

Kondziolka, J. M., & Nepf, H. M. (2014). Vegetation wakes and wake interaction shaping aquatic landscape evolution. *Limnology and Oceanography: Fluids and Environments*, *4*(1), 106–119. https://doi.org/10.1215/21573689-2846314

Kui, L., & Stella, J. C. (2016). Fluvial sediment burial increases mortality of young riparian trees but induces compensatory growth response in survivors. *Forest Ecology and Management*, *366*, 32–40. https://doi.org/10.1016/j.foreco.2016.02.001

Le Bouteiller, C., & Venditti, J. G. (2014). Vegetation-driven morphodynamic adjustments of a sand bed. *Geophysical Research Letters*, *41*(11), 3876–3883. https://doi.org/10.1002/2014gl060155

Leu, J. M., Chan, H. C., Jia, Y., He, Z., & Wang, S. S. (2008). Cutting management of riparian vegetation by using hydrodynamic model simulations. *Advances in Water Resources*, *31*(10), 1299–1308. https://doi.org/10.1016/j.advwatres.2008.06.001

Li, J., Claude, N., Tassi, P., Cordier, F., Crosato, A., & Rodrigues, S. (2020). Implementation of a novel approach accounting for the influence of vegetation on sediment transport in GAIA. In *Online proceedings of the papers submitted to the 2020 TELEMAC-MASCARET user conference october 2020* (pp. 2–8). Retrieved from https://henry.baw.de/bitstream/20.500.11970/107435/1/02-08_Li_proceedings_tuc_2020.pdf

Li, W. Q., Wang, D., Jiao, J. L., & Yang, K. J. (2019). Effects of vegetation patch density on flow velocity characteristics in an open channel. *Journal of Hydrodynamics*, *31*(5), 1052–1059. https://doi.org/10.1007/s42241-018-0086-6

Mahoney, J. M., & Rood, S. B. (1998). Streamflow requirements for cottonwood seedling recruitment—An integrative model. *Wetlands*, *18*(4), 634–645. https://doi.org/10.1007/BF03161678

Marsooli, R., & Wu, W. (2014). Numerical investigation of wave attenuation by vegetation using a 3D RANS model. *Advances in Water Resources*, *74*, 245–257. https://doi.org/10.1016/j.advwatres.2014.09.012

Meron, E. (2019). Vegetation pattern formation: The mechanisms behind the forms. *Physics Today*, *72*(11), 30–36. https://doi.org/10.1063/PT.3.4340

Murphy, E., Ghisalberti, M., & Nepf, H. (2007). Model and laboratory study of dispersion in flows with submerged vegetation. *Water Resources Research*, *43*(5). https://doi.org/10.1029/2006WR005229

Nagata, N., Hosoda, T., & Muramoto, Y. (2000). Numerical analysis of river channel processes with bank erosion. *Journal of Hydraulic Engineering*, *126*(4), 243–252. https://doi.org/10.1061/(ASCE)0733-9429(2000)126:4(243)

Nagata, N., Hosoda, T., Nakato, T., & Muramoto, Y. (2005). Three-dimensional numerical model for flow and bed deformation around river hydraulic structures. *Journal of Hydraulic Engineering*, *131*(12), 1074–1087. https://doi.org/10.1061/(ASCE)0733-9429(2005)131:12(1074)

Nepf, H. M. (1999). Drag, turbulence, and diffusion in flow through emergent vegetation. *Water Resources Research*, *35*(2), 479–489. https://doi.org/10.1029/1998WR900069

Nepf, H. M., & Vivoni, E. R. (2000). Flow structure in depth-limited, vegetated flow. *Journal of Geophysical Research*, *105*(C12), 28547–28557. https://doi.org/10.1029/2000JC900145

Nikuradse, J. (1950). Laws of flow in rough pipes. *NACA*.

Rominger, J. T., Lightbody, A. F., & Nepf, H. M. (2010). Effects of added vegetation on sand bar stability and stream hydrodynamics. *Journal of Hydraulic Engineering*, *136*(12), 994–1002. https://doi.org/10.1061/(ASCE)HY.1943-7900.0000215

Schwarz, C., Gourgue, O., Van Belzen, J., Zhu, Z., Bouma, T. J., Van De Koppel, J., et al. (2018). Self-organization of a biogeomorphic landscape controlled by plant life-history traits. *Nature Geoscience*, *11*(9), 672–677. https://doi.org/10.1038/s41561-018-0180-y

Shimizu, Y., Nelson, J., Arnez Ferrel, K., Asahi, K., Giri, S., Inoue, T., et al. (2020). Advances in computational morphodynamics using the International River Interface Cooperative (iRIC) software. *Earth Surface Processes and Landforms*, *45*(1), 11–37. https://doi.org/10.1002/esp.4653

Stone, B. M., & Shen, H. T. (2002). Hydraulic resistance of flow in channels with cylindrical roughness. *Journal of Hydraulic Engineering*, *128*(5), 500–506. https://doi.org/10.1061/(ASCE)0733-9429(2002)128:5(500)

Swartenbroekx, C., Soares-Frazão, S., Staquet, R., & Zech, Y. (2010). Two-dimensional operator for bank failures induced by water-level rise in dam-break flows. *Journal of Hydraulic Research*, *48*(3), 302–314. https://doi.org/10.1080/00221686.2010.481856

Tal, M., & Paola, C. (2010). Effects of vegetation on channel morphodynamics: Results and insights from laboratory experiments. *Earth Surface Processes and Landforms*, *35*(9), 1014–1028. https://doi.org/10.1002/esp.1908

Talmon, A. M., Struiksma, N., & Van Mierlo, M. C. L. M. (1995). Laboratory measurements of the direction of sediment transport on transverse alluvial-bed slopes. *Journal of Hydraulic Research*, *33*(4), 495–517. https://doi.org/10.1080/00221689509498657

Tsujimoto, T. (1999). Fluvial processes in streams with vegetation. *Journal of Hydraulic Research*, *37*(6), 789–803. https://doi.org/10.1080/00221689909498512

Van Dijk, W. M., Teske, R., Van de Lageweg, W. I., & Kleinhans, M. G. (2013). Effects of vegetation distribution on experimental river channel dynamics. *Water Resources Research*, *49*(11), 7558–7574. https://doi.org/10.1002/2013WR013574

Van Rijn, L. C. (1984). Sediment transport, part III: Bed forms and alluvial roughness. *Journal of Hydraulic Engineering*, *110*(12), 1733–1754. https://doi.org/10.1061/(asce)0733-9429(1984)110:12(1733)

Vargas-Luna, A., Crosato, A., Byshimo, P., & Uijttewaal, W. S. J. (2019). Impact of flow variability and sediment characteristics on channel width evolution in laboratory streams. *Journal of Hydraulic Research*, *57*(1), 51–61. https://www.tandfonline.com/doi/abs/10.1080/00221686.2018.1434836

Vargas-Luna, A., Duró, G., Crosato, A., & Uijttewaal, W. S. J. (2019). Morphological adaptation of river channels to vegetation establishment: A laboratory study. *Journal of Geophysical Research: Earth Surface*, *124*(7), 1981–1995. https://doi.org/10.1029/2018JF004878

Wintenberger, C. L., Rodrigues, S., Greulich, S., Bréhéret, J. G., Jugé, P., Tal, M., & Villar, M. (2019). Control of non-migrating bar morphodynamics on survival of populus Nigra seedlings during floods. *Wetlands*, *39*(2), 275–290. https://doi.org/10.1007/s13157-018-1121-7

Wu, W., Shields, F. D., Jr., Bennett, S. J., & Wang, S. S. (2005). A depth-averaged two-dimensional model for flow, sediment transport, and bed topography in curved channels with riparian vegetation. *Water Resources Research*, *41*(3). https://doi.org/10.1029/2004WR003730

Xu, Z. X., Ye, C., Zhang, Y. Y., Wang, X. K., & Yan, X. F. (2019). 2D numerical analysis of the influence of near-bank vegetation patches on the bed morphological adjustment. *Environmental Fluid Mechanics*, *20*(4), 1–32. https://doi.org/10.1007/s10652-019-09718-5

Zhang, M., Li, C. W., & Shen, Y. (2013). Depth-averaged modeling of free surface flows in open channels with emerged and submerged vegetation. *Applied Mathematical Modelling*, *37*(1–2), 540–553. https://doi.org/10.1016/j.apm.2012.02.049

Zhou, Y., Toda, Y., & Kubo, E. (2018). Distribution of initial vegetation recruitment on bare bar in sand bed river. *Journal of Water Resource and Protection*, *10*(04), 441–460. https://doi.org/10.4236/jwarp.2018.104024

Zong, L., & Nepf, H. (2011). Spatial distribution of deposition within a patch of vegetation. *Water Resources Research*, *47*(3). https://doi.org/10.1029/2010WR009516

Zong, L., & Nepf, H. (2012). Vortex development behind a finite porous obstruction in a channel. *Journal of Fluid Mechanics*, *691*, 368–391. https://doi.org/10.1017/jfm.2011.479